
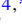




Nonadiabatic topological transfer in a nanomechanical phononic lattice

Tian Tian ^{1,2,3,*}, Han Cai ^{4,*}, Liang Zhang ⁵, Yichuan Zhang,^{3,6} Chang-Kui Duan,^{3,6} and Jingwei Zhou ^{3,6,†}

¹State Key Laboratory of Quantum Optics and Quantum Optics Devices, Institute of Opto-Electronics, Shanxi University, Taiyuan 030006, China


²Collaborative Innovation Center of Extreme Optics, Shanxi University, Taiyuan 030006, China

³CAS Key Laboratory of Microscale Magnetic Resonance and School of Physical Sciences, University of Science and Technology of China, Hefei 230026, China

⁴College of Optical Science and Engineering, State Key Laboratory of Extreme Photonics and Instrumentation, Zhejiang University, Hangzhou 310027, China

⁵Institute of Quantum Sensing, Zhejiang University, Hangzhou 310027, China

⁶CAS Center for Excellence in Quantum Information and Quantum Physics, University of Science and Technology of China, Hefei 230026, China

 (Received 4 October 2023; revised 25 January 2024; accepted 26 February 2024; published 15 March 2024)

Topologically protected boundary transport is a promising route to realize robust quantum manipulation between distant nodes. Conventional topological transports require a long transmission time to meet adiabatic evolution, which unfortunately becomes a significant obstacle for practical quantum systems with decoherence. Here, we report a fast and robust phonon transfer by breaking this adiabatic limitation in a one-dimensional nanomechanical topological interface lattice. The high-fidelity nonadiabatic topological transfer (NTT) can be predicted accurately via the localized mode and bulk levels. A dynamical method is then put forward to characterize the nonadiabatic oscillation of the NTT according to the chiral symmetry, and the oscillation of the instantaneous adiabaticity is measured by the phonon population on the even nanomechanical resonators. Furthermore, we confirm the robustness under various noises and the scalability of the NTT. Our results open the door to accelerating topological transport, which is valuable for developing fast and robust quantum information transfer protocols.

DOI: [10.1103/PhysRevB.109.125123](https://doi.org/10.1103/PhysRevB.109.125123)

I. INTRODUCTION

Transferring particles or states between distant nodes in a network is of fundamental importance in many areas of physics and engineering, including scalable quantum information processing [1–3]. Topological localized boundary modes provide an excellent carrier for transferring particles or quantum resources and have been introduced to design robust transfer passages in recent years [4–23]. Various adiabatic topological transfer (ATT) protocols [11–21] based on the one-dimensional Su-Schrieffer-Heeger (SSH) model [24] have been proposed. In these protocols, as shown in Fig. 1(a), the initial particle or quantum state follows the gap-protected localized mode $|\phi_0\rangle$ from one end transfer to the other via slowly varying the Hamiltonian in time. However, the fidelity of these ATTs will be harmed when the transfer process undergoes inevitable dissipations in a practical environment. Hence, an ideal topological transport requires not only robustness against local defects but also as fast as possible, especially for potential applications in quantum systems with finite lifetimes.

Different from ATTs, we notice that the transfer scheme “analogy to a big spin” [25–27] utilizes multilevel coherent

dynamics and takes a shorter time in lattice transports. However, due to the requirement of precise ratios in neighboring couplings, the “analogy to a big spin” transfer is sensitive to system imperfection. Inspired by the above, a natural question is whether one can use the advantage of coherent dynamics in multilevels to realize a fast topological transport.

Here, we propose a nonadiabatic topological transfer (NTT) protocol by combining the merits of multilevel coherent dynamics and spatial adiabatic passages. This fast and robust transfer is demonstrated in a phononic topological interface lattice, implemented through an array of nanomechanical resonators with real-time modulated parametric couplings. The process can be viewed as a hybrid ATT, during which the excited population is not irreversibly leaked but coherently oscillates between the topological zero-energy mode and engineered bulk states, schematically depicted in Fig. 1(b). Recently, by carefully designing the dispersion relation and utilizing nonadiabatic transitions, three-step and three-step up accelerated topological protocols were proposed in theory [14]. In this paper, we design a topological interface model with fully flat energy levels in a phononic lattice and obtain near-unit transfer fidelities with much shorter durations without entering the adiabatic regime in the experiment. These high-fidelity nonadiabatic transports can be predicted analytically by the flat topological structures.

To further characterize such a nonadiabatic process, we theoretically propose and experimentally verify a

*These authors contributed equally to this paper.

†zhoujw@ustc.edu.cn

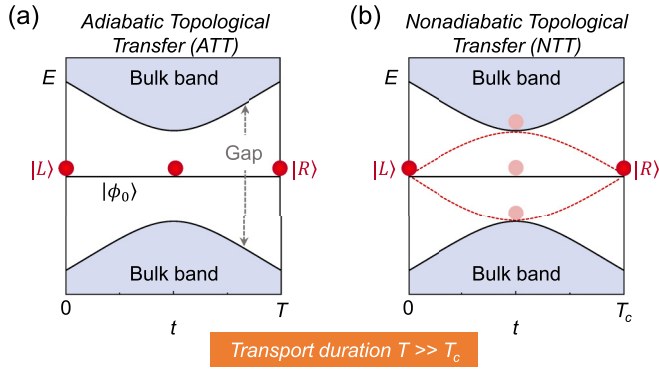


FIG. 1. Topological transfer mechanism. (a) A conventional topological transfer from the initial state $|L\rangle = |100 \dots 00\rangle$ to the target state $|R\rangle = |00 \dots 001\rangle$ adiabatically follows the midgap zero-energy mode $|\phi_0\rangle$. (b) A NTT with high fidelity is realized by breaking the adiabatic assumption. Nonadiabatic energy level transitions (dashed lines) between the zero-energy mode and the bulk levels are used to shorten the time consumption ($T_c \ll T$) and keep a near-unit transfer fidelity. Red balls stand for the probability distribution on instantaneous levels.

dynamical method to measure the population on the topological zero-energy mode, i.e., instantaneous adiabaticity, by

taking advantage of the chiral symmetry of the system. The instantaneous adiabaticity oscillates periodically as if a spin precessing in magnetic fields, unambiguously revealing the coherent and nonadiabatic features experimentally. Finally, we demonstrate the robustness and scalability of high-fidelity NTTs.

II. TOPOLOGICAL INTERFACE LATTICE

As shown in Fig. 2(a), we design and realize a one-dimensional phononic SSH lattice with $2N + 1$ harmonic oscillators. There are two nanomechanical resonators per unit cell. The intracell (intercell) hopping V_n (W_n) of the n th unit cell is controlled by parametric voltages $V_{ac} = V_{pk} \cos[(\omega_{2n} - \omega_{2n+1})t]$ (ω_i is the eigenfrequency of the i th resonator) and the fixed V_{dc} via Bias-Tees [17,28], see Fig. 2(b). Unlike the standard SSH model's uniform and alternate interactions, the intracell and intercell hoppings of the topological model we consider here are spatially inhomogeneous and temporally modulated [Fig. 2(c)]. It is noted that the inhomogeneous hoppings of this topological interface lattice are derived from the two-mode Jaynes-Cummings model (see Appendix A). According to the relation $V_n > W_n$ and $V_n < W_n$ of each cell at any moment, the lattice can be divided into two segments

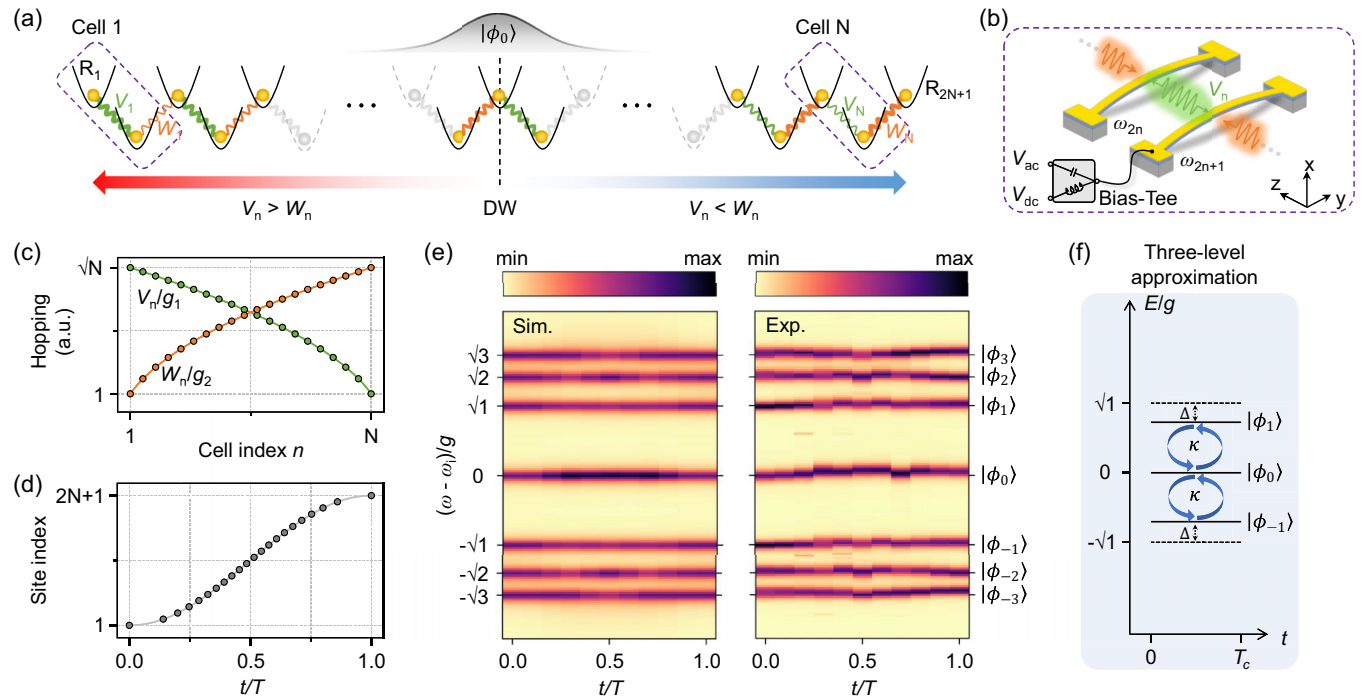


FIG. 2. Phononic implementation of the dynamic topological interface lattice. (a) The dynamic SSH interface lattice with $2N + 1$ harmonic oscillators. A zero-energy topological defect mode $|\phi_0\rangle$ is localized on the domain wall (DW), where the intercell hopping W_n is equal to the intracell hopping V_{n+1} . (b) A unit cell of the phononic lattice includes two doubly clamped nanomechanical resonators. The fundamental mode of each resonator is vibrational along the x axis. Couplings of adjacent resonators are controlled by parametric voltages $V_{ac} = V_{pk} \cos[(\omega_i - \omega_{i+1})t]$ together with stationary dc voltages via Bias-Tees. (c) The hoppings V_n and W_n are spatially distributed according to square-root laws and are temporally modulated by $g_1 = g \sin(\pi t/2T)$ and $g_2 = g \cos(\pi t/2T)$. (d) The localized mode $|\phi_0\rangle$ follows that the moving DW is an ATT. The gray line indicates the mean position of the mode $|\phi_0\rangle$. Dots mark the position of the DW, where $W_n = V_{n+1}$. We take $N = 20$ in (c) and (d). (e) Simulation (left) and experiment (right) of the eigenenergy spectrum of the dynamic SSH interface model in the phononic lattice with $N = 3$ and $g = 2\pi \times 63.5$ Hz. The experimental result is obtained from the response spectra of seven nanomechanical resonators. (f) The coherent dynamics of NTTs can be simplified to a three-level model consisting of $|\phi_0\rangle$ and $|\phi_{\pm 1}\rangle$ with the energy correction Δ and the nonadiabatic transition κ .

with distinct topological phases, and there is a domain wall (DW) at the interface $W_n = V_{n+1}$ [29]. Therefore, the above phononic lattice is termed the dynamic SSH interface model, and its Hamiltonian reads

$$\hat{H}(t) = \sum_{n=1}^N [V_n \hat{a}_{2n-1}^\dagger \hat{a}_{2n} + W_n \hat{a}_{2n}^\dagger \hat{a}_{2n+1} + \text{H.c.}], \quad (1)$$

where \hat{a}_n^\dagger (\hat{a}_n) is the creation (annihilation) operator of the n th phononic cavity, hoppings $V_n = \sqrt{N-n+1}g_1$ and $W_n = \sqrt{n}g_2$ with temporal factors $g_1 = g \sin(\pi t/2T)$, $g_2 = g \cos(\pi t/2T)$, and g is a constant.

Owing to the bulk-boundary correspondence, there is a zero-energy mode $|\phi_0\rangle$ localized at the DW. With real-time modulations, the localized mode $|\phi_0\rangle$ accompanied by the DW moves from the leftmost site $|L\rangle = |100 \cdots 00\rangle$ to the rightmost site $|R\rangle = |00 \cdots 001\rangle$ under a period T [Fig. 2(d)], forming an ATT. However, according to the description in Fig. 1(a), the adiabatic following $|\phi_0\rangle$ requires a very long transport duration T .

III. HIGH-FIDELITY NTTS

To highlight the nonadiabatic transition, it is convenient to expand a system state $|\psi\rangle = \sum_n c_n |\phi_n\rangle$ based on instantaneous eigenstates $|\phi_n\rangle$ with eigenenergies E_n . The evolution of the system is therefore governed by [30]

$$\partial_t c_n = -iE_n c_n - \sum_{m \neq n} c_m \kappa_{n,m}, \quad (2)$$

where $\kappa_{n,m} = -\kappa_{m,n}^* = \langle \phi_n | \partial_t H | \phi_m \rangle / (E_m - E_n)$ is the nonadiabatic transition rate between levels $|\phi_n\rangle$ and $|\phi_m\rangle$.

The nonadiabatic transition between instantaneous eigenmodes can be greatly simplified by the square-root hopping inhomogeneity. This lattice has a fully gapped flat-level structure with time-independent eigenenergies $E_{\pm n} = \pm \sqrt{n}g$ ($n = 0, 1, \dots, N$). In Fig. 2(e), we verify this flat-level structure and its square-root scaling by using seven nanomechanical resonators with real-time modulated parametric couplings, which correspond to a dynamic SSH interface model with $N = 3$. Specifically, we set $g = 2\pi \times 63.5$ Hz in the experiment. Seven frequency response spectra of all resonators are measured and normalized for each moment. The measured energy bands are an average result of these normalized spectra (see Appendix D).

In such a flat-level design, the only nonzero nonadiabatic transition rates between the topological zero-energy mode and the bulk modes are $\kappa_{0,\pm 1} = \pm \kappa = \pm \sqrt{N}\pi / (2\sqrt{2}T)$ [31–33]. The resultant simplified three-level Hamiltonian is

$$\hat{H}_{\text{eff}} = E'_{\pm 1} |\phi_{\pm 1}\rangle \langle \phi_{\pm 1}| + [\pm i\kappa |\phi_{\pm 1}\rangle \langle \phi_0| + \text{H.c.}], \quad (3)$$

with schematic diagram shown in Fig. 2(f). The eigenenergies of levels $|\phi_{\pm 1}\rangle$ is corrected as $E'_{\pm 1} = E_{\pm 1} \mp \Delta$, with $\Delta = 7(N-1)\pi^2 / (8T^2g)$ being the energy shift induced by higher-order nonadiabatic transitions (see Appendix A). Then, the population oscillation between $|\phi_0\rangle$ and $|\phi_{\pm 1}\rangle$ is governed by the pulse area,

$$A(N, T) = \Omega T, \quad (4)$$

which is similar to a spin-1 particle driven by a microwave pulse with a pulse duration T and a precession frequency $\Omega = \sqrt{2\kappa^2 + (g - \Delta)^2}$. According to the area theorem [34], the critical transport duration T_c is obtained when the pulse area A is an even multiple of π . Therefore, we can obtain high-fidelity NTTs by setting the critical duration T_c .

To demonstrate the fast topological passages, we carry out phonon transfer under the parameters $N = 3$ and $g = 2\pi \times 63.5$ Hz. Figure 3(a) displays the numerical and experimental results of the transfer fidelity as a function of the transport duration

$$\mathcal{F}(T) = |\langle R | \psi(T) \rangle|^2 = |\langle R | \hat{T} e^{-i \int_0^T d\tau \hat{H}(\tau)} | L \rangle|^2, \quad (5)$$

where $|R\rangle = |7\rangle = |0000001\rangle$ is the target state, $|L\rangle = |1\rangle = |1000000\rangle$ is the initial state, and \hat{T} is the time-ordering operator.

In the experiment, the initial state of the topological phononic lattice is created by exciting the first resonator at its phononic frequency, and initial coherent excitations are described by the vibration amplitude. We stress that the dissipation of all resonators can be regarded as a global factor and eliminated by vibration amplitude normalization [28,35]. Therefore, the evolution of normalized vibration amplitudes is determined by the conservative Hamiltonian $\hat{H}(t)$. Figure 3(e) shows the experimental result of the normalized vibration intensities for the NTT with $T_c = 33.7$ ms. The experimental result agrees with the numerical simulation of the single phonon probability distribution plotted in Fig. 3(f). In the same way, we study other NTTs in the phononic lattice. The experimental data of the transfer fidelity in Fig. 3(a) is given by the normalized vibration intensity of the seventh resonator. The error bar of each transfer fidelity is obtained by 200 repetitions. The black dashed line is the analytical result of the three-level approximation. It is clear that the transfer fidelity of NTTs with critical duration T_c can reach a unit which is far away from the adiabatic region.

IV. INSTANTANEOUS ADIABATICITY

To further evaluate these NTTs, we compute and measure the population on the zero-energy mode to quantify the instantaneous adiabaticity $P_0(t) = |\langle \phi_0(t) | \psi(t) \rangle|^2 = |c_0(t)|^2$ during the transport process. Figures 3(b)–3(d) illustrates three typical NTTs with pulse areas $A = 2\pi$, 3π , and 4π , respectively. For the high-fidelity NTTs ($T_c = 19.8$ ms and $T_c = 33.7$ ms) with even multiples of π of pulse areas, the oscillation of instantaneous adiabaticity unambiguously indicates that the population converges to the zero-energy mode at the end of transfers, leading to local maxima in Fig. 3(a). In contrast, the transport process with the 3π pulse area [Fig. 3(c)] has a local minimum of the transfer fidelity since the coherent population exchange between $|\phi_0\rangle$ and $|\phi_{\pm 1}\rangle$ is maximized at the end, which is demonstrated by P_0 as well as the calculated population evolution of $P_{\pm 1}(t) = |c_{\pm 1}(t)|^2$.

By taking advantage of the chiral symmetry of $\hat{H}(t)$, we measure the instantaneous adiabaticity (see Appendix E) according to

$$P_0(t) \approx 1 - \frac{2}{\tau_c} \int_0^{\tau_c} d\tau P_{\text{even}}(\tau; t), \quad (6)$$

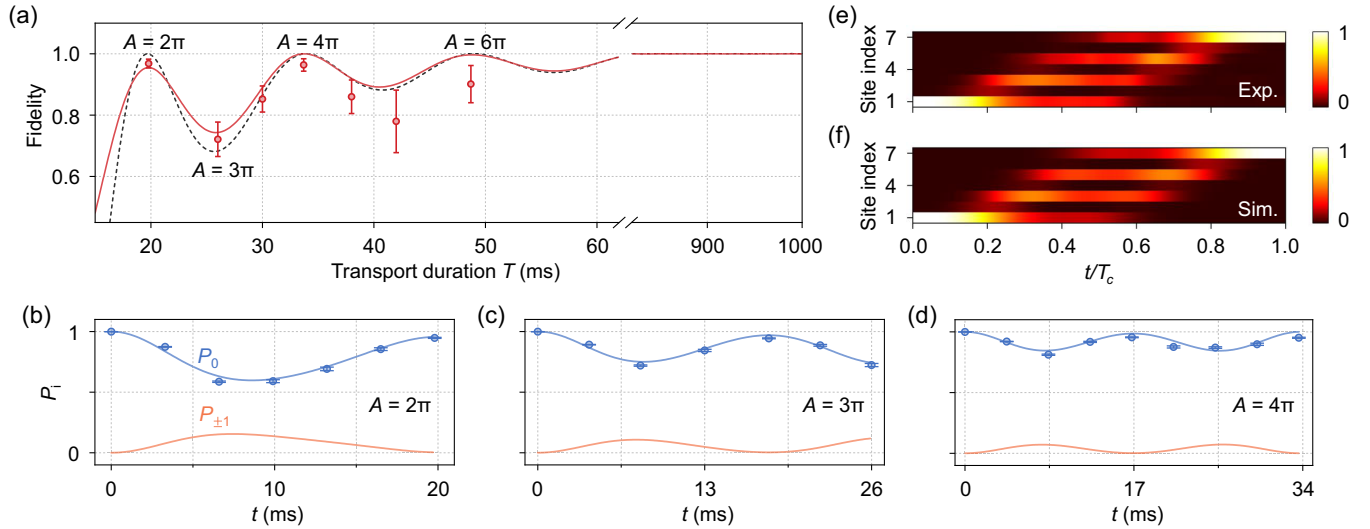


FIG. 3. Nonadiabatic topological transfer. (a) The fidelity is a function of the transfer duration. The red line is acquired from the numerical simulation of the time-dependent Schrödinger equation. The experimental data (red points) are obtained by the normalized vibration intensity of the nanomechanical resonator R_7 . The three-level approximation (dashed line) predicts NTTs. (b)–(d) The instantaneous adiabaticity $P_0 = |\langle \phi_0 | \psi \rangle|^2$ of three NTTs with $T = 19.8$ ms, 26.0 ms, and 33.7 ms, respectively. The experimental points are measured by the dynamical method [Eq. (6)]. For comparison, we numerically compute the population of the eigenmodes P_i ($i = 0, \pm 1$) in lines. All error bars in (a)–(d) represent the statistical confidence of one standard deviation. (e) Experimental result of the normalized vibration intensities of the seven nanomechanical resonators for the high-fidelity NTT with $T_c = 33.7$ ms. (f) Numerical simulation of the single phonon probability distribution under the same conditions as (e).

where a characteristic time $\tau_c = \pi/g$ and $P_{\text{even}}(\tau; t) = \sum_{n=1}^N |(2\mathbf{n}|e^{-i\hat{H}(t)\tau}|\psi(t))|^2$ is the total probability distribution on even sites for the state $|\psi(t)\rangle$ evolving for an extra time τ under the fixed Hamiltonian at the moment t . Taking the assumption that the population of the modes $|\phi_{\pm n}\rangle$ ($n \geq 2$) are negligible, $P_{\text{even}}(\tau; t) \approx (|c_1|^2 + |c_{-1}|^2)/2 - \text{Re}[c_1^* c_{-1} \exp(2ig\tau)]$ gives the population of $|\phi_{\pm 1}\rangle$ after integrating out the cross term (Appendix E). In other words, Eq. (6) reveals a dynamical method to measure the instantaneous adiabaticity. In the experiment, we keep all time-dependent couplings unchanged at one moment and then measure the vibration amplitudes in the next $\tau_c = 7.9$ ms. The probability distribution on even sites is acquired from the normalized vibration intensity of the resonators R_2, R_4 and R_6 . As shown in Figs. 3(b)–3(d), our experimental results (blue points) match the numerical results (blue lines) derived from the single phonon transfer very well.

V. ROBUSTNESS AND SCALABILITY

Since nonadiabatic tunnelings break the gap protection, there is a natural question of whether these high-fidelity NTTs are still robust. In the experiment, we deliberately add two types of impulse noises with strength Δ_{noise} into adjacent couplings for the NTT with $T_c = 33.7$ ms. For type-I noises, 1 ms square-wave pulses are applied on all interactions at the moment $t = 0.5T_c$. We test the transfer fidelity under different noise strengths Δ_{noise} and present the experimental data (blue points) in Fig. 4(a). Another type of impulse noise (type-II noise) appears at different moments of the six couplings, and the transfer fidelity is shown by green points in Fig. 4(b). In addition to impulse noises, the transfer fidelity is numerically

studied under white noises in Appendix F. Our results distinctly demonstrate that the high-fidelity NTT is still robust against these noises on control voltages.

Figure 4(c) shows the numerical result of NTTs for different site numbers. These fast topological passages match the prediction (black dashed lines) according to the pulse area of the three-level approximation. It is clear that these high-fidelity NTTs exist stably where the pulse area $A = 2\pi, 4\pi, 6\pi$, and so on.

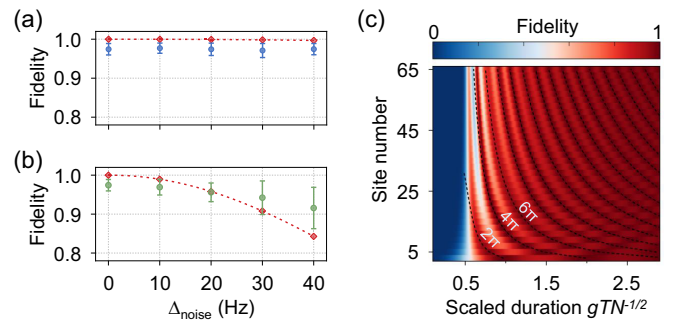


FIG. 4. Robustness and scalability. (a), (b) The fidelity of the NTT with $T_c = 33.7$ ms under the two kinds of impulse noises with diverse strengths. Type I: 1 ms square-wave pulses are applied on all adjacent interactions at the moment $t = 0.5T_c$. Type II: 1 ms impulse noises successively appear at $t = 0.3T_c, 0.5T_c, 0.7T_c, 0.3T_c, 0.5T_c$, and $0.7T_c$ for the six adjacent interactions. All error bars denote the statistical confidence of one standard deviation. Red rhombus and dashed lines are numerical results. (c) Calculated transfer fidelity of the dynamic topological lattice with different site numbers under the scaled duration gT/\sqrt{N} .

VI. SUMMARY AND DISCUSSION

We demonstrate a scalable, fast, and robust NTT protocol in a nanomechanical phononic lattice. The core of this fast topological transfer protocol is using the nonadiabatic transitions between the zero-energy mode and bulk levels. This scheme only relies on the experimentally accessible nearest-neighbor couplings in lattices and it does not require any additional interactions in the topological model [36]. Due to the fully flat-level structure of the dynamic SSH interface lattice, the high-fidelity NTTs can be predicted accurately. In addition, the symmetry-based dynamical method is proposed to characterize the instantaneous adiabaticity without complicated state tomography, which can be generalized to other topological transfer protocols with chiral symmetry [15,18,19]. Moreover, compared with conventional ATTs, the transfer time of NTTs is significantly reduced, which is essential for applications in quantum systems with finite lifetimes. Our experiment breaks the previously assumed adiabaticity in topological transports and takes a step toward exploring fast and robust transfer schemes for both classical excitations [10,18,37–39] and quantum resources such as spin [40], correlation [41,42], and entanglement [43–45].

ACKNOWLEDGMENTS

The authors acknowledge the support of the National Key Research and Development Program of China (Grants No. 2021YFB3202800 and No. 2018YFA0306600), the National Natural Science Foundation of China (Grants No. 12304566, No. 12374335, and No. U21A20437), the Chinese Academy of Sciences (Grants No. XDC07000000 and No. GJJSTD20200001), Anhui Initiative in Quantum Information Technologies (Grant No. AHY050000), Anhui Provincial Natural Science Foundation (Grant No. 2208085QA16), Fundamental Research Program of Shanxi Province (Grant No. 202303021221067), China Postdoctoral Science Foundation (Grants No. 2021M693094 and No. 2021M693096), the Hefei Comprehensive National Science Center and the Fundamental Research Funds for the Central Universities. This work was partially carried out at the USTC Center for Micro and Nanoscale Research and Fabrication.

APPENDIX A: MAPPING AND SOLVING THE SSH INTERFACE MODEL

The SSH interface model in the main text can be one-to-one mapped from a two-mode Jaynes-Cumming model [31] [see Fig. 5(a)], describing the coherent interaction between a two-level atom and two cavities. With the rotating wave approximation and the assumption that the cavity frequencies are on-resonant with the transition frequency of the atom, the Hamiltonian of the two-mode JC model is

$$H_{JC} = (g_1 \hat{a}_1 + g_2 \hat{a}_2)^\dagger \sigma_- + \text{H.c.}, \quad (\text{A1})$$

where $\sigma_- = |\downarrow\rangle\langle\uparrow|$ is the raising operator of a two-level atom with $|\uparrow\rangle$ being the atomic excited state and $|\downarrow\rangle$ being the atomic ground state, \hat{a}_i^\dagger ($i = 1, 2$) is the creation operator of the i th cavity and g_j is the vacuum Rabi frequency between the atom and the cavity, respectively. Since the total excitation number $N = p + n_1 + n_2$ is conserved ($p = 1$ for

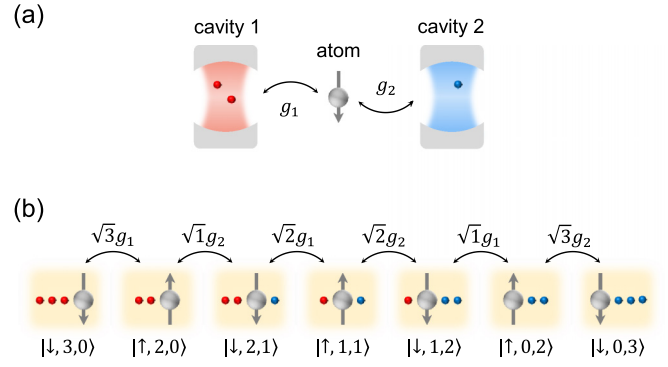


FIG. 5. Two-mode Jaynes-Cummings model. (a) Schematics of the two-mode Jaynes-Cummings model. (b) The Fock-state lattice ($N = 3$) of the Hamiltonian Eq. (A1). Each yellow shaded area indicates a Fock state $|\uparrow$ or $|\downarrow, n_1, n_2\rangle$, where red (blue) balls indicate the photons in each cavity, respectively.

the atomic excited state, $p = 0$ for the atomic ground state, and n_i is the photon number in the i th cavity), we can study the Hamiltonian in the subspace with different excitation numbers N separately, which consists of $2N + 1$ Fock states $\{|\uparrow$ or $|\downarrow, n_1, n_2\rangle\}$.

For a better understanding, we explicitly depict all the Fock states of the $N = 3$ subspace in Fig. 5(b). When the atom is in excited state ($p = 1$), there are three Fock states for two photons in two cavities, i.e., $|\uparrow, 2, 0\rangle$, $|\uparrow, 1, 1\rangle$, and $|\uparrow, 0, 2\rangle$. When the atom is in the atomic ground state ($p = 0$), three photons form four Fock states as $|\downarrow, 3, 0\rangle$, $|\downarrow, 2, 1\rangle$, $|\downarrow, 1, 2\rangle$, and $|\downarrow, 0, 3\rangle$. In the basis of the Fock states, the nonzero matrix elements of H_{JC} are

$$\begin{aligned} \langle\uparrow, n_1, n_2|H_{JC}|\downarrow, n_1 + 1, n_2\rangle &= \sqrt{n_1 + 1}g_1, \\ \langle\uparrow, n_1, n_2|H_{JC}|\downarrow, n_1, n_2 + 1\rangle &= \sqrt{n_2 + 1}g_2. \end{aligned} \quad (\text{A2})$$

It means that the Fock states are coupled alternatively to form a one-dimensional lattice in the Hilbert subspace. The featured square-root factors are attributed to the bosonic nature $\hat{a}_i|n_i\rangle = \sqrt{n_i}|n_i - 1\rangle$. By mapping each Fock state to a nanomechanical resonator and engineer the hopping strength according to Eq. (A2), we obtain the phononic lattice in the main text.

With the mapping, we are ready to solve the eigenenergy, eigenmodes as well as the nonadiabatic transition of the phononic lattice in the picture of JC model. The two-mode JC model can be rewritten as

$$H_{JC} = g\hat{b}^\dagger\sigma_- + \text{H.c.}, \quad (\text{A3})$$

where $\hat{b}^\dagger = g_1/g\hat{a}_1^\dagger + g_2/g\hat{a}_2^\dagger$ is the collective bright mode, accompanied by the collective dark mode $\hat{d}^\dagger = g_2/g\hat{a}_1^\dagger - g_1/g\hat{a}_2^\dagger$, and $g = \sqrt{g_1^2 + g_2^2}$. It provides an equivalent Fock-state basis to describe each subspace in the collective modes, $|\uparrow$ or $|\downarrow, n_b, n_d\rangle_c$, with n_b being the photon number in the collective bright mode and n_d being the photon number in the collective dark mode. The nonzero matrix element of H_{JC} in the collective mode $|\dots\rangle_c$:

$${}_c\langle\uparrow, n_b, n_d|H_{JC}|\downarrow, n_b + 1, n_d\rangle_c = \sqrt{n_b + 1}g. \quad (\text{A4})$$

We notice that the $2N + 1$ matrix contains $N \times 2 \times 2$ blocks and an uncoupled zero-energy dark state, i.e., the transfer channel

$$\begin{aligned}
|\phi_0\rangle &\equiv |\downarrow, 0, N\rangle_c \\
&= \frac{(\hat{d}^\dagger)^N}{\sqrt{N!}} |\downarrow, 0, 0\rangle_c \\
&= \frac{1}{\sqrt{N!}} \left(\frac{g_2}{g} \hat{a}_1^\dagger - \frac{g_1}{g} \hat{a}_2^\dagger \right)^N |\downarrow, 0, 0\rangle \\
&= \sum_{n=0}^N \sqrt{\frac{N!}{(N-n)!n!}} \left(\frac{g_2}{g} \right)^{N-n} \left(-\frac{g_1}{g} \right)^n |\downarrow, N-n, n\rangle \\
&\xrightarrow{\text{mapping}} \sum_{n=0}^N j_{2n+1} |\mathbf{2n+1}\rangle, \tag{A5}
\end{aligned}$$

where j_n is the phonon probability distribution on the n -th resonator. By diagonalizing the 2×2 blocks, we can also obtain the eigenstates $|\phi_{\pm n}\rangle$ ($n = 1, 2, \dots, N$),

$$|\phi_{\pm n}\rangle = \frac{1}{\sqrt{2}} (|\uparrow, n-1, N-n\rangle_c \pm |\downarrow, n, N-n\rangle_c), \tag{A6}$$

with eigenenergy $E_{\pm n} = \pm\sqrt{n}g$. The nonadiabatic transition is obtained by calculating the matrix element of

$$\begin{aligned}
\frac{\partial H}{\partial t} &= \frac{\pi}{2T} (g_2 \hat{a}_1 - g_1 \hat{a}_2)^\dagger \sigma_- + \text{H.c.} \\
&= \frac{\pi g}{2T} \hat{d}^\dagger \sigma_- + \text{H.c.}, \tag{A7}
\end{aligned}$$

with the nonzero elements

$$\begin{aligned}
\kappa_{0,\pm 1} &= \frac{\langle \phi_0 | \partial_t H | \phi_{\pm 1} \rangle}{E_{\pm 1} - E_0} = \pm \frac{\sqrt{N}\pi}{2\sqrt{2}T}, \\
\kappa_{n,\pm(n+1)} &= \frac{\langle \phi_n | \partial_t H | \phi_{\pm(n+1)} \rangle}{E_{\pm(n+1)} - E_n} = \frac{\sqrt{N-n}\pi}{4T(\pm\sqrt{n+1} - \sqrt{n})}, \\
\kappa_{-n,\pm(n+1)} &= \frac{\langle \phi_{-n} | \partial_t H | \phi_{\pm(n+1)} \rangle}{E_{\pm(n+1)} - E_{-n}} = \frac{\sqrt{N-n}\pi}{4T(\pm\sqrt{n+1} + \sqrt{n})}. \tag{A8}
\end{aligned}$$

APPENDIX B: THREE-LEVEL APPROXIMATION

To study the nonadiabatic dynamics, we treat the levels $|\phi_0\rangle$ and $|\phi_{\pm 1}\rangle$ as the system and all the other $(2N-2)$ eigenstates as the environment. The nonzero elements of the nonadiabatic coupling between the system and environment are

$$\begin{aligned}
\kappa_{1,\pm 2} &= \frac{\pm\sqrt{N-1}\pi}{4T(\pm\sqrt{2}-1)}, \\
\kappa_{-1,\pm 2} &= \frac{\pm\sqrt{N-1}\pi}{4T(\pm\sqrt{2}+1)}, \tag{B1}
\end{aligned}$$

The nonadiabatic transition introduces an energy correction to the level $|\phi_{\pm 1}\rangle$ as $E'_{\pm 1} = E_{\pm 1} + \delta E_{\pm 1}$ with the uncorrected

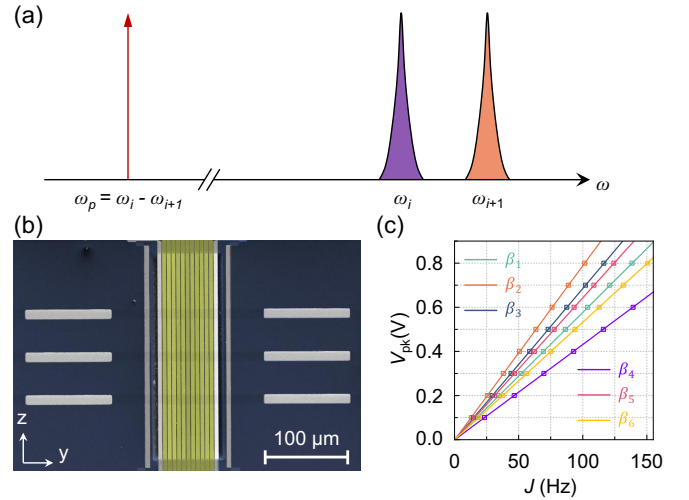


FIG. 6. Sample and parametric couplings. (a) Schematic of parametric couplings. (b) A false-color scanning electron micrograph of the doubly clamped nanomechanical resonators. The fundamental mode of each resonator is vibrational along the x axis. (c) The linear relationship between ac voltage amplitude V_{pk} and effective coupling J_i of neighboring nanomechanical resonators under $V_{dc} = 9.5$ V. The six slopes β_i are determined by fitting experimental data.

eigenenergies $E_{\pm n} = \pm\sqrt{n}g$ and

$$\begin{aligned}
\delta E_1 &= \frac{|\kappa_{1,2}|^2}{E_1 - E_2} + \frac{|\kappa_{1,-2}|^2}{E_1 - E_{-2}} = -\Delta, \\
\delta E_{-1} &= \frac{|\kappa_{-1,2}|^2}{E_{-1} - E_2} + \frac{|\kappa_{-1,-2}|^2}{E_{-1} - E_{-2}} = \Delta. \tag{B2}
\end{aligned}$$

In such a three-level approximation, the evolution of $|\psi\rangle = c_0|\phi_0\rangle + c_1|\phi_1\rangle + c_{-1}|\phi_{-1}\rangle$ is governed by the dynamic equations:

$$i \frac{d}{dt} \begin{pmatrix} c_1 \\ c_0 \\ c_{-1} \end{pmatrix} = \begin{pmatrix} g - \Delta & i\kappa & 0 \\ -i\kappa & 0 & i\kappa \\ 0 & -i\kappa & \Delta - g \end{pmatrix} \begin{pmatrix} c_1 \\ c_0 \\ c_{-1} \end{pmatrix}. \tag{B3}$$

The physics is the same as a spin-1 particle with spin matrices $\{S_x, S_y, S_z\}$ driven by a magnetic field $\{0, -\sqrt{2}\kappa, g - \Delta\}$, which is described by the Hamiltonian

$$H_{\text{spin-1}} = (g - \Delta)S_z - \sqrt{2}\kappa S_y. \tag{B4}$$

Based on the boundary conditions $c_0(t=0) = 1$ and $c_{\pm 1}(t=0) = 0$, we obtain

$$P_0(t) = |c_0|^2 = [(g - \Delta)^2 + 2\kappa^2 \cos(\Omega t)]^2 / \Omega^4, \tag{B5}$$

which reaches local maxima when ΩT_c is an even multiple of π with the spin precession frequency $\Omega = \sqrt{2\kappa^2 + (g - \Delta)^2}$.

APPENDIX C: EXPERIMENTAL SETUP

A false-color scanning electron micrograph of the doubly clamped nanomechanical resonator array is shown in Fig. 6(b). The size of each doubly clamped resonator is 240 μm long, 5 μm wide, and 100 nm thick. The space of adjacent nanomechanical resonators is about 600 nm. The sample

TABLE I. First-order vibrational modes of the nanomechanical resonators (77 K and 3.3×10^{-8} mbar). These parameters were measured before applying V_{dc} .

Resonators i	Frequency $\omega_i/2\pi$ (kHz)	Bandwidth $\gamma_i/2\pi$ (Hz)
1	748.367	11.3
2	739.464	11.5
3	725.260	11.0
4	737.842	12.3
5	740.331	11.3
6	734.532	11.4
7	748.971	11.2

was placed in a vacuum chamber with 3.3×10^{-8} mbar at the liquid-nitrogen temperature. The inevitable fabrication errors lead to a minor difference in phononic frequencies, which provides a chance to realize interactions between these nanomechanical resonators via the parametric coupling illustrated in Fig. 6(a). In particular, as shown in Fig 2(b), we add a parametric voltage $V_{ac} = V_{pk} \cos(\omega_p t)$ and a dc voltage $V_{dc} = 9.5$ V in a side of the i th resonator by a Bias-Tee. The other side of the i th resonator is in series with a high resistance to generate potential differences with adjacent nanomechanical resonators. By controlling the electrostatic parametric frequency ω_p and the amplitude V_{pk} , we can realize tunable couplings of adjacent resonators at different sites. Similar details of the nanomechanical device and the experimental circuits were introduced elsewhere [28,35]. In this experiment, we utilize seven first-order vibrational modes of these neighboring resonators to carry out the dynamically modulated SSH interface lattice with $N = 3$. Their frequencies and damping parameters are listed in Table I. Table II and Fig. 6(c) display the six linear relations between the ac voltage amplitude V_{pk} and the effective coupling of the nanomechanical resonator array.

APPENDIX D: ENERGY BAND STRUCTURE

In frames rotating at ω_i , the phonon-number-preserving Hamiltonian of seven coupled nanomechanical resonators reads

$$\hat{H}_{\text{eff}}(t) = \sum_{i=1}^6 J_i(t) (\hat{a}_i^\dagger \hat{a}_{i+1} + \hat{a}_i \hat{a}_{i+1}^\dagger), \quad (\text{D1})$$

where \hat{a}_i^\dagger (\hat{a}_i) is the creation (annihilation) operator of the i th phononic mode. Since all dissipations γ_i are nearly identical and the maximum value of $T(\gamma_i - \gamma_j)/2\pi < 1$ for any transfer duration T in experiment, the normalized measurement results could characterizes this conservative Hamiltonian. As described in the main text, the dynamic SSH interface lattice

TABLE II. Linear coefficient β_i between voltage $V_{pk}^{i,i+1}$ and effective coupling J_i .

i	1	2	3	4	5	6
β_i (mV/Hz)	5.78	7.90	6.88	4.32	6.44	5.32

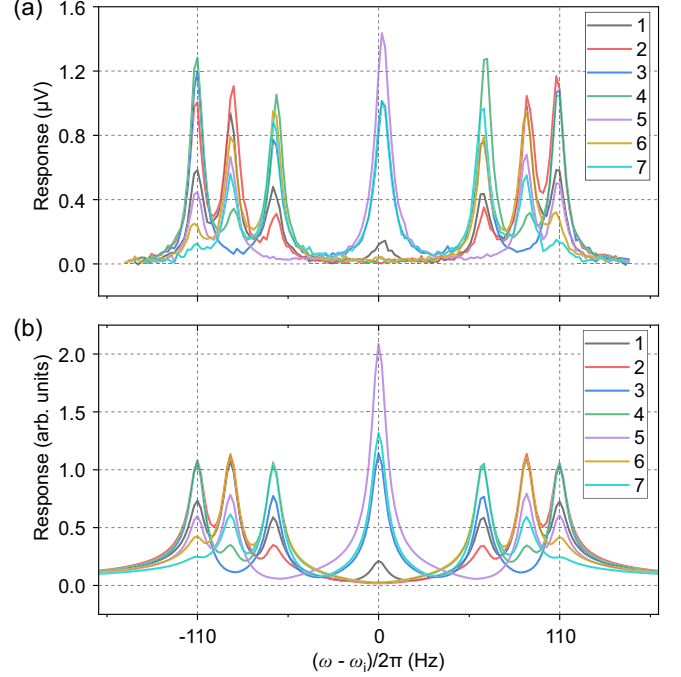


FIG. 7. Band structures. Experiment (a) and simulation (b) of frequency response curves of the seven nanomechanical resonators at the moment $t = 0.6T$. The coupling constant $g = 2\pi \times 63.5$ Hz.

is implemented by applying real-time varying parametric voltages according to the time-dependent couplings in Eq. (1) and the coefficient β_i in Table II.

We measured the band structure in Fig. 2(e) to confirm the topological phononic lattice. Taking Fig. 7(a) as an example, we measure the frequency response spectrums of the seven resonators by lock-in amplifiers under the six adjacent couplings $J_i(t)$ at $t = 0.6T$. The mechanical density of state at this moment can be further obtained by cumulating the normalized response spectra. For comparison, we also simulate the response spectra by using parameters of these nanomechanical resonators and show the results in Fig. 7(b).

APPENDIX E: CHIRAL SYMMETRY AND INSTANTANEOUS ADIABATICITY

Like the normal 1D SSH model [29], the chiral operator of the topological interface lattice with $2N + 1$ sites can be defined as

$$\hat{\Gamma} = \hat{P}_o - \hat{P}_e, \quad (\text{E1})$$

where $\hat{P}_o = \sum_{n=0}^N |2\mathbf{n} + \mathbf{1}\rangle \langle 2\mathbf{n} + \mathbf{1}|$ and $\hat{P}_e = \sum_{n=1}^N |2\mathbf{n}\rangle \langle 2\mathbf{n}|$ are the two orthogonal sublattice projectors and they satisfy the relation

$$\hat{P}_o + \hat{P}_e = \hat{I}, \quad \hat{P}_o \cdot \hat{P}_e = 0. \quad (\text{E2})$$

Here \hat{I} is the identity operator. The chiral operator also fulfils $\hat{\Gamma}^\dagger \hat{\Gamma} = \hat{\Gamma}^2 = \hat{I}$.

For the dynamic SSH interface lattice, the chiral symmetry persists because

$$\hat{\Gamma} \hat{H} \hat{\Gamma}^\dagger = -\hat{H} \quad (\text{E3})$$

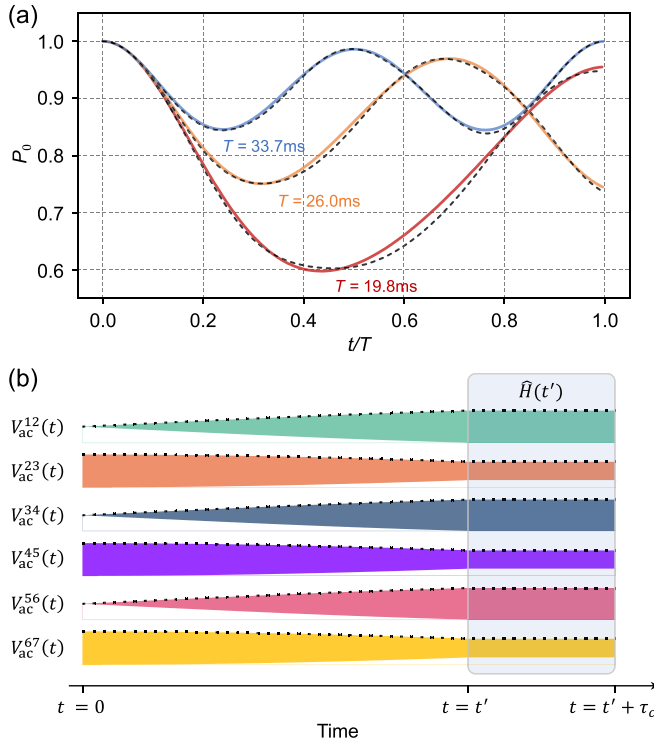


FIG. 8. Instantaneous adiabaticity and experimental measurements. (a) The instantaneous adiabaticity $P_0(t)$ of various transfer durations T . The solid lines stand for the numerical results from $P_0(t) = |\langle \phi_0(t) | \psi(t) \rangle|^2$. The dashed lines are obtained from the dynamical method of Eq. (E13) with $\tau_c = 7.9$ ms. (b) The schematic of experimental sequences of parametric voltages $V_{ac}^{ij}(t) = V_{pk}^{ij}(t) \cos[(\omega_i - \omega_j)t]$ for measuring the instantaneous adiabaticity. The dashed outline indicates the time-varying amplitude $V_{pk}^{ij}(t)$.

always does for any moment of the Hamiltonian $\hat{H}(t)$ in the main text. It gives rise to the symmetric energy spectrum, i.e., there must be another eigenenergy $-E_n$ for any eigenenergy E_n of $\hat{H}(t)$. In addition, the corresponding eigenstate $|\phi_{\pm n}\rangle$ of $E_{\pm n}$ obeys $|\phi_{\pm n}\rangle = \hat{\Gamma}|\phi_{\mp n}\rangle$ for $E_n \neq 0$. Due to the chiral symmetry, the topological zero-energy state $|\phi_0\rangle$ of the topological lattice only supports the odd sublattice.

Next, we consider the evolution of the initial state $|L\rangle$ under the Hamiltonian $\hat{H}(t)$. At the moment t , the instantaneous state $|\psi(t)\rangle = \hat{\mathcal{T}}e^{-i\int_0^t d\tau \hat{H}(\tau)}|L\rangle$ can be expressed as

$$|\psi(t)\rangle = c_0|\phi_0(t)\rangle + \sum_{m=1}^N (c_m|\phi_m(t)\rangle + c_{-m}|\phi_{-m}(t)\rangle), \quad (\text{E4})$$

where $|\phi_0(t)\rangle$ and $|\phi_{\pm m}(t)\rangle$ are the instantaneous eigenstates of $\hat{H}(t)$. Therefore, the probability of the sublattice projector \hat{P}_e is

$$P_{\text{even}}(t) = \langle \psi(t) | \hat{P}_e | \psi(t) \rangle. \quad (\text{E5})$$

By utilizing the relation $\hat{P}_e = \frac{1}{2}(\hat{\Gamma} - \hat{\Gamma}^\dagger)$ and $|\phi_m\rangle = \hat{\Gamma}|\phi_{-m}\rangle$, Eq. (E5) can be simplified as

$$P_{\text{even}}(t) = \frac{1}{2} \sum_{m=1}^N (|c_m|^2 + |c_{-m}|^2 - 2\text{Re}[c_m^* c_{-m}]). \quad (\text{E6})$$

If the state $|\psi(t)\rangle$ further evolves an extra time τ at the fixed Hamiltonian $\hat{H}(t)$, the state $|\varphi(\tau; t)\rangle = e^{-i\hat{H}(t)\tau}|\psi(t)\rangle$ can be expressed as

$$|\varphi(\tau; t)\rangle = \sum_{m=1}^N (c_m e^{-iE_m \tau} |\phi_m(t)\rangle + c_{-m} e^{iE_m \tau} |\phi_{-m}(t)\rangle) + c_0 |\phi_0(t)\rangle, \quad (\text{E7})$$

and the probability on the even sublattice reads

$$P_{\text{even}}(\tau; t) = \langle \varphi(\tau; t) | \hat{P}_e | \varphi(\tau; t) \rangle = \frac{1}{2} \sum_{m=1}^N (|c_m|^2 + |c_{-m}|^2) - \sum_{m=1}^N \text{Re}[c_m^* c_{-m} e^{2iE_m \tau}]. \quad (\text{E8})$$

In the same way, we can get the probability on the odd sublattice:

$$P_{\text{odd}}(\tau; t) = |c_0|^2 + \frac{1}{2} \sum_{m=1}^N (|c_m|^2 + |c_{-m}|^2) + \sum_{m=1}^N \text{Re}[c_m^* c_{-m} e^{2iE_m \tau}]. \quad (\text{E9})$$

Because the tunneling of nonadiabatic topological passages principally occurs at the energy levels E_0 and $E_{\pm 1}$, the

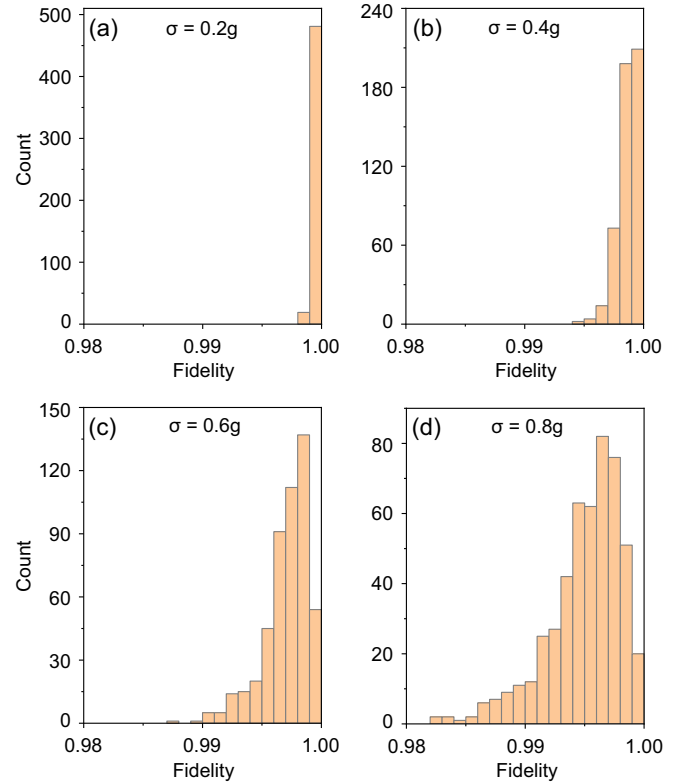


FIG. 9. Robustness against white noises. The fidelity of the fast nonadiabatic topological transfer with $T_c = 33.7$ ms under Gaussian white noises with diverse strengths. For each standard deviation σ , random noises were chosen from 500 groups to calculate the transfer fidelity numerically.

probabilities of Eqs. (E8) and (E9) can be simplified in a three-level condition, i.e.,

$$P_{\text{even}}(\tau; t) \approx \frac{1}{2} (|c_1|^2 + |c_{-1}|^2) - \text{Re}[c_1^* c_{-1} e^{2iE_1\tau}], \quad (\text{E10})$$

$$P_{\text{odd}}(\tau; t) \approx \frac{1}{2} (|c_1|^2 + |c_{-1}|^2) + |c_0|^2 + \text{Re}[c_1^* c_{-1} e^{2iE_1\tau}]. \quad (\text{E11})$$

Hence, the instantaneous adiabaticity $P_0(t) = |c_0|^2$ can be measured by a dynamical method of the population on even sites because of

$$P_0(t) \approx 1 - \frac{2}{\tau_c} \int_0^{\tau_c} d\tau P_{\text{even}}(\tau; t), \quad (\text{E12})$$

where $\tau_c = \pi/E_1 = \pi/g$ is the characteristic time.

Figure 8(a) compares the numerical results (solid lines) from $P_0(t) = |\langle \phi_0(t) | \psi(t) \rangle|^2$ with the simulations (dashed lines) according to the dynamical method

$$P_0(t) \approx 1 - \frac{2}{\tau_c} \int_0^{\tau_c} d\tau \sum_{n=1}^N |\langle 2\mathbf{n} | \varphi(\tau; t) \rangle|^2 \quad (\text{E13})$$

for different transfer durations T with $N = 3$ and $\tau_c = 7.9$ ms.

To measure the instantaneous adiabaticity $P_0(t)$ of different nonadiabatic topological passages, we design and apply the parametric voltage sequences in the experiment. As shown in Fig. 8(b), the dynamically modulated parametric voltages V_{ac}^{ij} are fixed at any moment t and persist $\tau_c = 7.9$ ms. According to the summation of normalized vibration intensities on the even resonators during this period τ_c , the instantaneous adiabaticity is calculated by Eq. (E13).

APPENDIX F: ROBUSTNESS AGAINST WHITE NOISES

In the experiment, two types of impulse noises are chosen to test the transfer fidelity of the fast NTT with $T_c = 33.7$ ms. As shown in Fig. 9, we also numerically check the robustness of this fast transfer passage under Gaussian white noises. In particular, we add random noises on each real-time modulated coupling (i.e., W_n and V_n) of the dynamic SSH interface lattice in the time domain. Every set of the random noise on each coupling obeys a Gaussian distribution $\mathcal{N}(0, \sigma^2)$. We choose 500 groups for each standard deviation σ . It is clear that the nonadiabatic transfer keeps near-unit fidelity, even the standard deviation $\sigma = 0.8g$.

-
- [1] C. H. Bennett and D. P. DiVincenzo, Quantum information and computation, *Nature (London)* **404**, 247 (2000).
- [2] H. J. Kimble, The quantum internet, *Nature (London)* **453**, 1023 (2008).
- [3] T. E. Northup and R. Blatt, Quantum information transfer using photons, *Nat. Photonics* **8**, 356 (2014).
- [4] Y. E. Kraus, Y. Lahini, Z. Ringel, M. Verbin, and O. Zeitler, Topological states and adiabatic pumping in quasicrystals, *Phys. Rev. Lett.* **109**, 106402 (2012).
- [5] N. Y. Yao, C. R. Laumann, A. V. Gorshkov, H. Weimer, L. Jiang, J. I. Cirac, P. Zoller, and M. D. Lukin, Topologically protected quantum state transfer in a chiral spin liquid, *Nat. Commun.* **4**, 1585 (2013).
- [6] S. Nakajima, T. Tomita, S. Taie, T. Ichinose, H. Ozawa, L. Wang, M. Troyer, and Y. Takahashi, Topological Thouless pumping of ultracold fermions, *Nat. Phys.* **12**, 296 (2016).
- [7] M. Lohse, C. Schweizer, O. Zeitler, M. Aidelsburger, and I. Bloch, A Thouless quantum pump with ultracold bosonic atoms in an optical superlattice, *Nat. Phys.* **12**, 350 (2016).
- [8] Y. Ke, X. Qin, F. Mei, H. Zhong, Y. S. Kivshar, and C. Lee, Topological phase transitions and Thouless pumping of light in photonic waveguide arrays, *Laser Photonics Rev.* **10**, 995 (2016).
- [9] Z. G. Chen, W. Tang, R.-Y. Zhang, Z. Chen, and G. Ma, Landau-Zener transition in the dynamic transfer of acoustic topological states, *Phys. Rev. Lett.* **126**, 054301 (2021).
- [10] Y. Xia, E. Riva, M. I. N. Rosa, G. Cazzulani, A. Erturk, F. Braghin, and M. Ruzzene, Experimental observation of temporal pumping in electromechanical waveguides, *Phys. Rev. Lett.* **126**, 095501 (2021).
- [11] N. Lang and H. P. Büchler, Topological networks for quantum communication between distant qubits, *npj Quantum Inf.* **3**, 47 (2017).
- [12] F. Mei, G. Chen, L. Tian, S.-L. Zhu, and S. Jia, Robust quantum state transfer via topological edge states in superconducting qubit chains, *Phys. Rev. A* **98**, 012331 (2018).
- [13] S. Longhi, Topological pumping of edge states via adiabatic passage, *Phys. Rev. B* **99**, 155150 (2019).
- [14] I. Brouzos, I. Kiorpelidis, F. K. Diakonov, and G. Theoharis, Fast, robust, and amplified transfer of topological edge modes on a time-varying mechanical chain, *Phys. Rev. B* **102**, 174312 (2020).
- [15] N. E. Palaio dimopoulos, I. Brouzos, F. K. Diakonov, and G. Theoharis, Fast and robust quantum state transfer via a topological chain, *Phys. Rev. A* **103**, 052409 (2021).
- [16] J. Yuan, C. Xu, H. Cai, and D.-W. Wang, Gap-protected transfer of topological defect states in photonic lattices, *APL Photonics* **6**, 030803 (2021).
- [17] T. Tian, Y. Zhang, L. Zhang, L. Wu, S. Lin, J. Zhou, C.-K. Duan, J.-H. Jiang, and J. Du, Experimental realization of nonreciprocal adiabatic transfer of phonons in a dynamically modulated nanomechanical topological insulator, *Phys. Rev. Lett.* **129**, 215901 (2022).
- [18] W. Liu, C. Wu, Y. Jia, S. Jia, G. Chen, and F. Chen, Observation of edge-to-edge topological transport in a photonic lattice, *Phys. Rev. A* **105**, L061502 (2022).
- [19] T. Yuan, C. Zeng, Y.-Y. Mao, F.-F. Wu, Y.-J. Xie, W.-Z. Zhang, H.-N. Dai, Y.-A. Chen, and J.-W. Pan, Realizing robust edge-to-edge transport of atomic momentum states in a dynamically modulated synthetic lattice, *Phys. Rev. Res.* **5**, L032005 (2023).
- [20] X. Zhao, Y. Xing, J. Cao, S. Liu, W.-X. Cui, and H.-F. Wang, Engineering quantum diode in one-dimensional time-varying superconducting circuits, *npj Quantum Inf.* **9**, 59 (2023).
- [21] C. Wu, W. Liu, Y. Jia, G. Chen, and F. Chen, Observation of topological pumping of a defect state in a Fock photonic lattice, *Phys. Rev. A* **107**, 033501 (2023).

- [22] J. Zurita, C. E. Creffield, and G. Platero, Fast quantum transfer mediated by topological domain walls, *Quantum* **7**, 1043 (2023).
- [23] L. Huang, Z. Tan, H. Zhong, and B. Zhu, Fast and robust quantum state transfer assisted by zero-energy interface states in a splicing Su-Schrieffer-Heeger chain, *Phys. Rev. A* **106**, 022419 (2022).
- [24] W. P. Su, J. R. Schrieffer, and A. J. Heeger, Solitons in polyacetylene, *Phys. Rev. Lett.* **42**, 1698 (1979).
- [25] R. J. Cook and B. W. Shore, Coherent dynamics N -level atoms and molecules. III. An analytically soluble periodic case, *Phys. Rev. A* **20**, 539 (1979).
- [26] M. Christandl, N. Datta, A. Ekert, and A. J. Landahl, Perfect state transfer in quantum spin networks, *Phys. Rev. Lett.* **92**, 187902 (2004).
- [27] M. B. Plenio, J. Hartley, and J. Eisert, Dynamics and manipulation of entanglement in coupled harmonic systems with many degrees of freedom, *New J. Phys.* **6**, 36 (2004).
- [28] T. Tian, Y. Ke, L. Zhang, S. Lin, Z. Shi, P. Huang, C. Lee, and J. Du, Observation of dynamical phase transitions in a topological nanomechanical system, *Phys. Rev. B* **100**, 024310 (2019).
- [29] J. K. Asbóth, L. Oroszlány, and A. Pályi, *A Short Course on Topological Insulators*, Lecture Notes in Physics, Vol. 919 (Springer, New York, 2016).
- [30] J. J. Sakurai and J. Napolitano, *Modern Quantum Mechanics* (Cambridge University Press, Cambridge, UK, 2020).
- [31] E. T. Jaynes and F. W. Cummings, Comparison of quantum and semiclassical radiation theories with application to the beam maser, *Proc. IEEE* **51**, 89 (1963).
- [32] H. Cai and D. W. Wang, Topological phases of quantized light, *Nat. Sci. Rev.* **8**, nwaa196 (2021).
- [33] J. Deng, H. Dong, C. Zhang, Y. Wu, J. Yuan, X. Zhu, F. Jin, H. Li, Z. Wang, H. Cai, C. Song, H. Wang, J. Q. You, and D. W. Wang, Observing the quantum topology of light, *Science* **378**, 966 (2022).
- [34] M. O. Scully and M. S. Zubairy, *Quantum Optics* (Cambridge University Press, Cambridge, UK, 1997).
- [35] S. Lin, L. Zhang, T. Tian, C.-K. Duan, and J. Du, Dynamic observation of topological soliton states in a programmable nanomechanical lattice, *Nano Lett.* **21**, 1025 (2021).
- [36] F. M. D'Angelis, F. A. Pinheiro, D. Guéry-Odelin, S. Longhi, and F. Impens, Fast and robust quantum state transfer in a topological Su-Schrieffer-Heeger chain with next-to-nearest-neighbor interactions, *Phys. Rev. Res.* **2**, 033475 (2020).
- [37] E. Riva, M. I. N. Rosa, and M. Ruzzene, Edge states and topological pumping in stiffness-modulated elastic plates, *Phys. Rev. B* **101**, 094307 (2020).
- [38] J. Cao, W.-X. Cui, X. X. Yi, and H.-F. Wang, Controllable photon-phonon conversion via the topologically protected edge channel in an optomechanical lattice, *Phys. Rev. A* **103**, 023504 (2021).
- [39] L.-S. Zeng, Y.-X. Shen, Y.-G. Peng, D.-G. Zhao, and X.-F. Zhu, Selective topological pumping for robust, efficient, and asymmetric sound energy transfer in a dynamically coupled cavity chain, *Phys. Rev. Appl.* **15**, 064018 (2021).
- [40] C. Schweizer, M. Lohse, R. Citro, and I. Bloch, Spin pumping and measurement of spin currents in optical superlattices, *Phys. Rev. Lett.* **117**, 170405 (2016).
- [41] T. Haug, L. Amico, L.-C. Kwek, W. J. Munro, and V. M. Bastidas, Topological pumping of quantum correlations, *Phys. Rev. Res.* **2**, 013135 (2020).
- [42] W. Kao, K.-Y. Li, K.-Y. Lin, S. Gopalakrishnan, and B. L. Lev, Topological pumping of a 1D dipolar gas into strongly correlated prethermal states, *Science* **371**, 296 (2021).
- [43] F. Yang, S. Yang, and L. You, Quantum transport of Rydberg excitons with synthetic spin-exchange interactions, *Phys. Rev. Lett.* **123**, 063001 (2019).
- [44] S. Tan, R. W. Bomantara, and J. Gong, High-fidelity and long-distance entangled-state transfer with Floquet topological edge modes, *Phys. Rev. A* **102**, 022608 (2020).
- [45] C. Wang, L. Li, J. Gong, and Y.-x. Liu, Arbitrary entangled state transfer via a topological qubit chain, *Phys. Rev. A* **106**, 052411 (2022).